Supporting Information

Luk et al. 10.1073/pnas.1312437110

SI Text

SI Methods

Chemicals. ^{15}N-ammonium chloride, [$^{13}C_6$,$^{2}H_7$]-glucose, 99.9 atom% $^{2}H_2O$, and folate were purchased from Sigma. NADPH, $NADP^+$, and isopropyl-β-D-thiogalactopyranoside (IPTG) were purchased from Melford. H_2F was prepared by dithionite reduction of folate (1). The concentrations of NADPH and H_2F were determined spectrophotometrically, using extinction coefficients of 6,200 $M^{-1}\cdot cm^{-1}$ at 339 nm and 28,000 $M^{-1}\cdot cm^{-1}$ at 282 nm, respectively (2).

Enzyme Preparation. *Escherichia coli* dyhydrofolate reductase (EcDHFR) and ^{15}N-, ^{13}C-, ^{2}H-labeled (heavy) EcDHFR in M9 medium were prepared using a modification of the protocol described by Falzone et al. (3). *E. coli* BL21(DE3) cells harboring a cDNA for EcDHFR (4) from an overnight culture in LB medium containing 100 μg/mL ampicillin were washed three times with M9 medium and then grown in 1 L M9 medium until the OD_{600} reached 0.6. IPTG (to 0.5 mM) was added and the culture grown to an OD_{600} of 2.0. The cells were harvested and the enzyme was purified as previously described (5). Heavy EcDHFR was produced as described for the unlabeled enzyme in M9 medium in [$^{2}H_2$, 99.9 atom%] H_2O supplemented with 1 g/L [^{15}N, 98 atom%] NH_4Cl and 2 g/L [$^{13}C_6$, 99 atom%; 1,2,3,4,5,6,6-$^{2}H_7$, 97 atom%] glucose. In both cases, "normal" water (i.e., $^{1}H_2O$) was used for purification, so all exchangeable deuterons were replaced by protons. The purity of the enzyme was assessed by SDS/PAGE. Typically ∼30 mg of apparently homogenous EcDHFR was obtained from 1 L culture. Enzymes were stored at 4 °C for up to 3 wk without detectable loss of activity. Electrospray ionization mass spectrometry indicated masses of 17,996.5 and 19,933.6 Daltons for light and heavy enzymes, respectively.

Circular Dichroism Spectroscopy. Circular dichroism experiments were performed on an Applied PhotoPhysics Chirascan spectrometer, using 14 μM protein in deoxygenated 10 mM potassium phosphate buffer (pH 7). Spectra (Fig. S1) were measured between 200 nm and 400 nm in 10-mm quartz cuvettes under N_2 with 50 nm/min scan speed, 0.5 nm data pitch, 1 nm bandwidth, and 0.5 s response time.

Steady-State Kinetic Measurements. Steady-state kinetic measurements (Table S1) were performed on a JASCO V-660 spectrophotometer as described in ref. 6, monitoring the decrease in absorbance at 340 nm during the reaction [ε_{340} (NADPH + H_2F) = 11,800 $M^{-1}\cdot cm^{-1}$] (7). The steady-state turnover rates of EcDHFR were determined at pH 7 and pH 9.5 in MTEN buffer (50 mM morpholinoethanesulfonic acid, 25 mM Tris, 25 mM ethanolamine, 100 mM NaCl, and 10 mM β-mercaptoethanol), using 30 nM enzyme. The pH was carefully adjusted at each experimental temperature to account for the temperature dependence of the pK_a of organic amines. The enzyme was preincubated with NADPH (100 μM) at the desired temperature for 5 min before addition of H_2F (100 μM). Each data point is the result of three independent measurements. To determine Michaelis constants (Table S2), concentrations of NADPH were varied between 3 μM and 100 μM (pH 7) or between 1 μM and 100 μM (pH 9.5), and concentrations of H_2F were varied between 0.5 μM and 100 μM, while keeping the concentration of the other reactant fixed at 100 μM.

Pre–Steady-State Kinetic Measurements. Hydride transfer rate constants (Tables S1 and S3) were measured under single-turnover conditions on a Hi-Tech Scientific stopped-flow spectrophotometer essentially as described before (8). Before mixing, the enzyme (40 μM) was preincubated with NADPH (16 μM) for at least 1 min in 100 mM potassium phosphate containing 100 mM NaCl and 10 mM β-mercaptoethanol at pH 7 or in MTEN buffer for pH-dependent measurements, and the reaction started by rapidly mixing with H_2F (200 μM) in the same buffer. Where MTEN buffer was used, the pH was carefully adjusted at each experimental temperature to account for the temperature dependence of the pK_a of organic amines. Reduction of the fluorescence resonance energy transfer from the enzyme to NADPH during the reaction was measured by exciting the sample at 297 nm and measuring emission using a 400-nm cutoff filter. All measurements were repeated at least six times. Rate constants were extracted by fitting the kinetic data to the equation for a double-exponential decay.

Tunneling Model Fitting Methodology

Using Eq. **3** in the main text, we fitted the temperature-dependent experimental hydride transfer data at different values of pH (pH 7 fits used the pre–steady-state data, and pH 9.5 fits used the steady-state data). $\kappa^{HE}(T)$ and $\kappa^{LE}(T)$ were calculated using an analytic approximation to average energy-dependent Wentzel–Kramers–Brillouin (WKB) transmission coefficients over a thermal Maxwell–Boltzmann distribution (assuming a parabolic barrier shape) (9),

$$\kappa^{\ell}(T) = \frac{\beta}{\beta-\alpha^{\ell}}\left[\exp\left[\left(\beta-\alpha^{\ell}\right)V^{TS}\right]-1\right], \qquad \textbf{[S1]}$$

where ℓ is an index that denotes the heavy or light enzyme (HE or LE). V^{TS} is the classical transition-state energy, which is uncorrected for zero point energy and thus identical for both isotopomers within the Born–Oppenheimer approximation. $\alpha^{\ell} = 2\pi/(\hbar\omega^{\ell})$, where ω^{ℓ} is the angular velocity corresponding to the transition state frequency (i.e., $\omega = 2\pi\nu$, where ν is the magnitude of the transition-state imaginary frequency), and $\beta = (kT)^{-1}$.

Fitting to the data obtained at each pH was carried out using a nonlinear least-squares minimization algorithm where the total value of χ^2 was calculated using the light enzyme hydride transfer rate constants, $k^{LE}(T)$; the heavy enzyme hydride transfer rate constants, $k^{HE}(T)$; and the corresponding (enzyme) kinetic isotope effects (KIEs), $k^{LE}(T)/k^{HE}(T)$. Each of these datasets is depicted in Fig. 2 of the main text. To reduce the fitting parameter space, we followed similar procedures to those in our previous work (10, 11) and rationally constrained the parameters in Eq. **3** and Eq. **S1** as follows:

i) For light isotope systems, the transition state imaginary frequency generally has a larger magnitude than it does in heavy systems, indicating more significant curvature on the potential energy surface in mass-weighted coordinates. Thus, we specified that $\omega^{LE} \geq \omega^{HE}$, with 1,000 $cm^{-1} < \omega^{LE} < 4{,}000$ cm^{-1}. This range of values is typical of hydride transfer systems (11–14).

ii) Light isotope systems often have a smaller effective ε (enthalpic activation barrier) owing to larger zero-point energies in the reactant vibrations that take the system across the barrier and into the products. Hence we specified that $\varepsilon^{HE} \geq \varepsilon^{LE}$, with both within 10% of V^{TS}.

iii) C^{LE} and C^{HE}, which include the partition function ratio of the transition state to the reactant as well as the recrossing coefficient, differ by no more than an order of magnitude. The typical ratio of vibrational partition functions for isotopically and nonisotopically substituted harmonic oscillators is usually close to unity, far smaller than our constraint.

Even with these constraints, it was initially difficult to converge the fits owing to strong parameter codependencies, as discussed previously (11). The classical barrier height, V^{TS}, is among the most important parameters to derive from the fitting; however, a range of different parameter sets gave reasonably good fits with different values of V^{TS}. In light of this fact, we calculated values of χ^2 by scanning over fixed values of V^{TS}, with all other parameters floated. The fitting method indicates that our fits using Eq. **3** and Eq. **S1** for both pH 7 and pH 9.5 data give χ^2 minima when V^{TS} values are around 15 kcal·mol^{-1} (Fig. S2), in good agreement with the barrier from the classical potential of mean force (PMF) obtained independently from the quantum mechanics/molecular mechanics (QM/MM) molecular dynamics (MD) simulations. Using this optimal V^{TS} value, the best-fit parameters are shown in Table S4, and the corresponding fits produced by these parameters are shown in Fig. 2 of the main text. Our fitting procedure gives excellent agreement with experiment over the entire temperature range, but it is important to note that it yields considerable parameter codependency, so that the fitted values must be treated with caution (particularly for the pH 7 data). The results presented in Table S4 are our "best-fit" parameters insofar as they yield a minimum χ^2 value over the experimental data points, but a range of parameter combinations would have also produced reasonable fits. The large error bars in some of the parameters are really indicative of significant parameter covariance. This is not an inherent limitation of the fitting procedure: For example, more data would make it possible to better constrain the fits. Nevertheless, the most notable outcome from the fits is the fact that (*i*) they differ considerably from results obtained using an Arrhenius-type fit, and (*ii*) they agree very well with the results obtained from QM/MM calculations.

We note that it would have been possible to fit the data with a more sophisticated multistate (multiconformation) model of the sort required to explain the data in some other enzymes (10, 11); however, in the case of heavy and light DHFR, the multiple-conformer models did not give improved nonlinear least-squares fits compared with single-conformer models. This finding, alongside the good agreement with both experiment and QM/MM simulations based on a single-protein conformation, argues against the involvement of multiple significantly different conformations in the hydride transfer catalyzed by DHFR. Although the fits do not allow us to rule out the presence of multiple conformers conclusively, we are able to state with confidence that the experimental data here can be fitted just as well with a single-conformer model as with a multiconformer model.

QM/MM Ensemble-Averaged Variational Transition-State Theory Calculations and Molecular Dynamics Simulations

The Simulation Model. The starting structure for dynamics simulations was obtained from Protein Data Bank entry 3QL3 for the ternary complex EcDHFR·NADP$^+$·folate (15). The PROPKA3 program (16–19) was used to estimate the pK_a values of the titratable protein residues to verify their protonation states at pH 7; histidines 45, 114, and 141 were doubly protonated whereas all other histidine residues were protonated only on Nδ or Nε. To neutralize the system, 13 sodium counterions were placed in optimal electrostatic positions around the enzyme. Finally, the system was solvated using a cubic box of TIP3P (transferable intermolecular potential 3 point) water molecules with side lengths of 65.2 Å; water molecules with an oxygen atom within 2.8 Å of any heavy atom were removed. The full system contained 27,219 atoms, containing the protein (159 residues, 2,544 atoms), the substrate and cofactor (52 and 74 atoms, respectively), 13 sodium ions, and 8,196 water molecules (24,132 atoms). Heavy EcDHFR was prepared by modifying the masses of all ^{14}N, ^{12}C, and nonexchangeable ^{1}H atoms to those of ^{15}N, ^{13}C, and ^{2}H. The ratio between the masses of the simulated heavy and light enzymes was 1.10987, similar to the experimentally observed molecular weight increase.

The whole system was divided into a QM part and an MM part to perform combined QM/MM calculations (Fig. S3). The quantum subsystem contained 76 atoms, including parts of the cofactor (nicotinamide ring and the ribose) and substrate (pteridine ring and the *N*-methylene-substituted *p*-aminobenzoyl, pABA). Two hydrogen "link" atoms (20) were used to saturate the valence at the QM-MM boundary (Fig. S3). The quantum atoms were treated by the AM1 (Austin Method 1) Hamiltonian (21), modified using specific reaction parameters (denoted as AM1-SRP) developed previously for DHFR (22). The protein atoms and the ions were described by the OPLS-AA (Optimized Potentials for Liquid Simulations - All Atoms) (23) force field whereas the water molecules were described by the TIP3P potential (24). Cutoffs for the nonbonding interactions were applied using a switching function within a radius range of 13.0–9.0 Å. Periodic boundary conditions were used within the minimum image convention in all of the simulations.

PMF. One-dimensional PMFs, W^{CM}, were computed using the antisymmetric combination of distances describing the hydride transfer, $z = d_{C4Ht}–d_{HtC6}$, as the reaction coordinate. The umbrella sampling approach (25) was used, with the system restrained to remain close to the desired value of the reaction coordinate by means of the addition of a harmonic potential with a force constant of 2,500 kJ·mol^{-1}·A^{-2}, which allows good overlap between windows. The reaction coordinate was then explored in a range from –2.07 Å to 1.57 Å, with a window width of 0.07 Å (the total number of windows was 53). The probability distributions obtained from MD simulations within each individual window were combined by means of the weighted histogram analysis method (WHAM) (26). Twenty picoseconds of relaxation and 40 ps of production MD, with a time step of 0.5 fs, in the canonical ensemble [NVT (number, volume, temperature), with a reference temperature of 300 K] and the Langevin–Verlet integrator (27), were used in the simulations.

Five additional PMFs were computed at the AM1-SRP/MM level to check the robustness of our method. The starting structures were selected from snapshots of a long QM/MM MD simulation with the reaction coordinate restrained to the value obtained for the transition state (TS) of the first PMF. The results (Fig. S4*A*) show very small deviations between the profiles and between the averaged structures of the three states involved in the reaction (i.e., all of the reactant structures are similar, all of the TSs are similar to one another, and all of the product states are similar to one another). From these PMFs, the classical mechanical activation free-energy barrier, $W^{\ddagger}$, is 15.8 ± 0.4 kcal·mol^{-1}. In addition to being in good agreement with the fits to the experimental data, the values of $W^{\ddagger}$ are similar to previous PMF calculations (see, for example, refs. 22, 28, 29) It is important to note that the ensemble-averaged variational transition-state theory (EA-VTST) QM/MM calculations were performed for the fully protonated substrate. Therefore, it is appropriate to compare the EA-VTST rate constants with experimental results obtained at pH lower than 6 (*Discussion* in the main text). These values of the rate constants are expected to be approximately fivefold larger than those measured at pH 7 but the corresponding differences in terms of free energies would be smaller than 1 kcal·mol^{-1} (30).

Selected geometries of the reactant state (RS) and the TS were used as starting points to run 2-ns AM1-SRP/MM MD simulations with the reaction coordinate restrained to the corre-

sponding values, to investigate the structural properties of the RS and the TS in more detail. The average values of key geometrical parameters are listed in Table S5. The TS is at a value of the reaction coordinate close to zero (–0.17 Å), with the transferred hydrogen atom slightly closer to the donor carbon atom than to the acceptor one. As expected, the TS is characterized by a shorter distance between the donor and acceptor atoms (2.63 Å) than in the RS (3.93 Å), as well as a more linear arrangement of the three atoms directly involved in the transfer (C_{donor}-H-$C_{acceptor}$ equal to 163° and 141° in the TS and RS, respectively). It is noticeable that some H-bonding groups (Asp27, Ala7, and, in particular, Met20) significantly approach the reacting system as the reaction progresses: Comparing simulations of the RS and the TS, two new H-bonds are established between the sulfur atom of Met20 and N7N and N5 of nicotinamide ring and pteridine ring, respectively, at the TS. The effect of stronger interactions with the amide group of a nicotinamide ring cofactor at the TS than at the RS, already observed in simulations in our laboratory in the study of the hydride transfer between the formate anion and NAD^+ catalyzed by formate dehydrogenase (31), suggests a more stabilizing pattern of interactions in the TS than in the Michaelis complex.

Reactive Trajectory (Activated Dynamics) Simulations. We ran a 2-ns NVT QM/MM MD trajectory restrained to the TS region with a time step of 0.5 fs for the reaction in both enzymes. The simulation temperature was 300 K and one configuration was saved every 10 ps, resulting in 200 configurations that were used to compute free (unrestrained) downhill trajectories. The velocity associated with the reaction coordinate is not properly thermalized in these initial configurations (because of the reaction coordinate restraint). Thus, following a procedure similar to that used by Gao and coworkers (32) and used in our previous studies (31, 33–35), we selectively removed the projection of the velocity on the reaction coordinate and added a random value taken from a Maxwell–Boltzmann distribution.

For each of the saved TS configurations with modified velocities, we ran free molecular dynamics simulations (i.e., with no reaction coordinate restraint) within the microcanonical ensemble (NVE). Separately, for each configuration we integrated the equations of motion forward and backward, just changing the sign of the velocity components. Downhill trajectories were propagated from –2 ps to +2 ps, using a time step of 0.5 fs. The trajectories obtained were then classified as reactive trajectories when reactants connect to products (RP trajectories) or nonreactive trajectories leading either from reactants to reactants (RR) or from products to products (PP). Both reactive and nonreactive trajectories may exhibit recrossings of the dividing surface. To compute the recrossing transmission coefficient, we used the "positive flux" formulation (36), assuming that the trajectory is initiated at the barrier top with forward momentum along the reaction coordinate,

$$\gamma(t) = \frac{\langle j_+ \theta[z(+t)] \rangle - \langle j_+ \theta[z(-t)] \rangle}{\langle j_+ \rangle}, \qquad \textbf{[S2]}$$

where z is the reaction coordinate, j_+ represents the initially positive flux at $t = 0$, given by $z(t = 0)$, and $\theta(z)$ is a step function equal to one in the product side of the reaction coordinate and zero on the reactant side. The average is calculated over all of the trajectories.

Ensemble-Averaged Variational Transition-State Theory. Deviations from classical TST as a result of quantum tunneling effects can be estimated by means of EA-VTST (37–39). In this approach, the theoretical estimation of the rate constant can be written as

$$k_{theor}(T) = \Gamma(T) \frac{k_B T}{h} \exp\left(-\frac{\Delta G^{QC}_{act}}{RT}\right). \qquad \textbf{[S3]}$$

ΔG^{QC}_{act} is the quasiclassical activation free energy at the transition state, obtained from the classical mechanical (CM) PMF and including a correction for quantizing the vibrations orthogonal to the reaction coordinate and the vibrational free energy of the reactant mode that correlates with motion along the reaction coordinate, and is calculated as

$$\Delta G^{QC}_{act} = \left[W^{CM}(T, z^*) + \Delta W_{vib}(T, z^*)\right] - \left[W^{CM}(T, z_R) + \Delta W_{vib,R}(T) + G^{CM}_{R,T,F}\right], \qquad \textbf{[S4]}$$

where $\Delta W_{vib}(T, z^*)$ corrects $W^{CM}(T, z^*)$ to account for quantized vibrations orthogonal to z, the reaction coordinate along which the PMF is defined, at the maximum of the PMF, z^*; $\Delta W_{vib,R}(T)$ corrects $W^{CM}(T, z_R)$ for quantized vibrations at the reactant side minimum of the PMF, z_R, and $G^{CM}{}_{R,T,F}$ is a correction for the vibrational free energy of the reactant mode that correlates with motion along the reaction coordinate (37).

To correct the classical mechanical PMF, W^{CM}, normal mode analyses were performed for the quantum region atoms. ΔG^{QC}_{act}, as described elsewhere (37), is obtained by Eq. **S4**, with the terms defined above. Briefly, the zero-point energy for each mode within the primary zone is obtained by evaluating an ensemble average over primary subsystems and making a quasiharmonic approximation. At each ensemble point, we form a Hessian and project out the reaction coordinate. This allows one to obtain the corresponding vibrational frequencies at each point along the reaction path, averaged over an ensemble that includes the effects of anharmonicity. Quantization of the vibrational frequencies is then obtained as a correction to the classical PMF. In the reactants, zero-point energy is included in the reaction coordinate mode; at the TS, tunneling along the reaction coordinate mode is treated using the small curvature tunneling approximation. To perform these calculations, we localized 13 TS structures, starting from different configurations of the corresponding simulation windows in the heavy and light enzymes. After intrinsic reaction coordinate (IRC) calculations, we optimized the corresponding reactant structures and obtained the Hessian matrix for all of the stationary structures. The final quantum mechanical corrections were obtained as an average over these structures. $W^{‡}$, the PMF difference between the TS and the reactants [$W^{‡} = W^{CM}(T, z^*) - W^{CM}(T, z_R)$], was found to be 15.8 ± 0.4 kcal·mol^{-1}; $G^{CM}{}_{R,T,F}$, the vibrational free energy corresponding to the reaction coordinate at the reactants, was found to be 0.38 ± 0.02 kcal·mol^{-1}; and ΔW_{vib} (T), the correction for quantized vibrations [ΔW_{vib} $(T) = \Delta W_{vib}$ $(T, z^*) - \Delta W_{vib,R}$ (T)], was found to be −1.59 ± 0.10 kcal·mol^{-1}. Further corrections can be found in Table 1 of the main text. The quasiclassical free-energy barrier (i.e., the free energy corrected using zero point energy contributions) and the tunneling contributions, κ, are statistically indistinguishable in the light and heavy enzymes, owing to the fact that the primary zones of the heavy and light enzymes are effectively identical, because only the protein environment (and not the substrate/cofactor) was isotopically substituted in these simulations.

The transmission coefficient, Γ, is obtained as the product of recrossing (γ) and tunneling (κ) contributions:

$$\Gamma(T) = \gamma(T) \cdot \kappa(T). \qquad \textbf{[S5]}$$

The recrossing transmission coefficient, γ, was calculated by randomizing the reaction coordinate velocity for 200 TS configurations, running free downhill MD trajectories and using the positive flux formulation to calculate flux–flux correlation functions (Eq. **S2**).

The tunneling transmission coefficient, κ, was calculated with the small-curvature tunneling (SCT) approximation, which includes reaction-path curvature appropriate for enzymatic hydride transfers (40, 41). Previously, the SCT approximation has been applied successfully to enzymatic reactions, catalyzed by DHFR and aromatic amine dehydrogenase, and produced KIEs and phenomenological activation energies that are in good agreement with the experimental results (40, 41). The final tunneling contribution is obtained as the average over the reaction paths of 13 TS structures.

To test whether the position of the variational transition state is sensitive to the isotope substitution in the light and heavy systems, we expanded the original primary zone beyond the QM atoms of the substrate and cofactor, to include additional nearby residues (ALA7, MET20, ASP27, TYR100, ILE14, and ALA19). The internal reaction coordinate was then followed by stepping along the mass-weighted minimum energy path and reoptimizing both the primary and the secondary regions at each point. Geometry optimizations used a full Hessian in the primary region and gradients within the secondary region. We then added in the effects of mode quantization along the IRC as discussed above. The positions of the free-energy maxima (and thus the variational TS) are essentially identical for the light and heavy enzymes (Fig. S4*B*).

Finally, Eq. **S3** can be transformed into Eq. **S6** by incorporating the transmission coefficient into the exponential term, giving a phenomenological free energy of activation, ΔG_{eff}:

$$k_{\mathrm{theor}}(T) = \frac{k_{\mathrm{B}}T}{h}\exp\left(-\frac{\Delta G_{\mathrm{eff}}}{RT}\right). \qquad \textbf{[S6]}$$

Eq. **S6** folds in effects due to the transmission coefficient as corrections to the effective classical free-energy barrier.

In both the light and the heavy enzymes, the EA-VTST simulations give transmission coefficients reasonably close to unity, indicating that the simple reaction coordinate used here provides an accurate quantitative description of the chemical reaction; if other coordinates were significantly involved, the transmission coefficient would to be considerably smaller than unity (40).

It is important to note that the activated trajectories procedure described above for calculating γ varies slightly from the original EA-VTST prescription (39). That work outlines two different contributions to γ. First is the "stage 2 step 1" transmission coefficient, which is calculated using an ensemble of individual minimum energy paths (MEPs) within a frozen secondary zone. The extent to which individual MEPs vary from the PMF corresponds to how strongly the distinguished reaction coordinate is coupled to other modes within the primary zone. The second contributor to γ in the original EA-VTST framework is the so-called "stage 3" correction, which accounts for the free-energy change of the secondary zone as the system leaves the primary zone variational TS.

The principal difference between the two-stage transmission coefficient procedure outlined in the original EA-VTST procedure and the activated trajectories approach is that the latter allows a straightforward and simultaneous treatment of relaxation within both the primary and the secondary regions. For the system under investigation in this work, we judged this to be a particularly important aspect of the system, because the bulk of the isotopic substitution is within the secondary zone (i.e., the substrate/cofactor upon which the heavy and light proteins act is not isotopically substituted, making the primary zones of the heavy and light enzymes largely identical). Nevertheless, both approaches accomplish a similar goal, and the extent to which the recrossing coefficient deviates from unity provides a metric for how strongly coupled other degrees of freedom are to the distinguished reaction coordinate.

The question of whether the activated trajectories approach can help us to improve the definition of the reaction coordinate is certainly an interesting one. In principle, it should be possible to use our approach to improve the reaction coordinate definition (see, e.g., refs. 33 and 35). Diagonalization of primary zone Hessians might allow resolution of the features in the friction spectrum (Fig. S4*D*). However, for this system, we anticipate that such attempts will be fraught with substantial difficulties for two reasons: (*i*) The friction spectrum (Fig. S4*D*) shows that the most significant differences in heavy/light motions coupled to the hydride transfer reaction coordinate occur below 550 cm^{-1}; and (*ii*) Fig. S4 *E*–*G* shows that the difference in relaxation between the heavy and the light protein environment is difficult to see from inspecting individual dynamical motions; rather, the difference in protein response time can be seen only when one considers a large collection of atomic positions (e.g., in Fig. S4*H*). Both of these facts point to the reaction coordinate being coupled to collective low-frequency protein motions, and it is unlikely that diagonalization of a Hessian for sequentially larger subsets of the atoms surrounding the active space would allow assignment of these motions. Such analyses are usually accurate only for higher-frequency motions.

Calculation of the Friction Spectra. The dynamical coupling of protein motions to the reaction coordinate z can be analyzed in terms of a time-dependent friction $\zeta(t)$ that opposes to the advance of the system along the reaction coordinate. The friction kernel, $\zeta(t)$, can be obtained from the autocorrelation of the forces projected on the reaction coordinate (F_z) obtained from simulations where the system is kept at $z = z^*$ (42),

$$\zeta(t) = \frac{\langle F_z(0)F_z(t)\rangle_{z=z^*}}{\mu_z k_{\mathrm{B}}T}, \qquad \textbf{[S7]}$$

where k_{B} is the Boltzmann constant, T is the temperature, and μ_z is the reduced mass associated with the reaction coordinate. The friction spectrum is then obtained as the Fourier transform of the friction kernel and informs us about the frequency distribution of those motions coupled to the reaction coordinate.

1. Blakley RL (1960) Crystalline dihydropteroylglutamic acid. *Nature* 188:231–232.
2. Swanwick RS, Maglia G, Tey LH, Allemann RK (2006) Coupling of protein motions and hydrogen transfer during catalysis by Escherichia coli dihydrofolate reductase. *Biochem J* 394(Pt 1):259–265.
3. Falzone CJ, et al. (1994) 1H, 15N and 13C resonance assignments, secondary structure, and the conformation of substrate in the binary folate complex of Escherichia coli dihydrofolate reductase. *J Biomol NMR* 4(3):349–366.
4. Swanwick RS, Shrimpton PJ, Allemann RK (2004) Pivotal role of Gly 121 in dihydrofolate reductase from *Escherichia coli*: The altered structure of a mutant enzyme may form the basis of its diminished catalytic performance. *Biochemistry* 43(14):4119–4127.
5. Hay S, et al. (2009) Are the catalytic properties of enzymes from piezophilic organisms pressure adapted? *ChemBioChem* 10(14):2348–2353.
6. Evans RM, et al. (2010) Catalysis by dihydrofolate reductase from the psychropiezophile *Moritella profunda*. *ChemBioChem* 11(14):2010–2017.
7. Stone SR, Morrison JF (1982) Kinetic mechanism of the reaction catalyzed by dihydrofolate reductase from *Escherichia coli*. *Biochemistry* 21(16):3757–3765.
8. Maglia G, Allemann RK (2003) Evidence for environmentally coupled hydrogen tunneling during dihydrofolate reductase catalysis. *J Am Chem Soc* 125(44):13372–13373.
9. Skodje RT, Truhlar DG (1981) Parabolic tunneling calculations. *J Phys Chem* 85:624–628.
10. Glowacki DR, Harvey JN, Mulholland AJ (2012) Protein dynamics and enzyme catalysis: The ghost in the machine? *Biochem Soc Trans* 40(3):515–521.
11. Glowacki DR, Harvey JN, Mulholland AJ (2012) Taking Ockham's razor to enzyme dynamics and catalysis. *Nat Chem* 4(3):169–176.
12. Tresadern G, et al. (2002) Calculations of hydrogen tunneling and enzyme catalysis: A comparison of liver alcohol dehydrogenase, methylamine dehydrogenase and soybean lipoxygenase. *Chem Phys Lett* 358:489–494.
13. Temelso B, Sherrill CD, Merkle RC, Freitas RA, Jr. (2006) High-level ab initio studies of hydrogen abstraction from prototype hydrocarbon systems. *J Phys Chem A* 110(38): 11160–11173.
14. Alhambra C, Corchado JC, Sanchez ML, Gao JL, Truhlar DG (2000) Quantum dynamics of hydride transfer in enzyme catalysis. *J Am Chem Soc* 122:8197–8203.

15. Bhabha G, et al. (2011) A dynamic knockout reveals that conformational fluctuations influence the chemical step of enzyme catalysis. *Science* 332(6026):234–238.
16. Li H, Robertson AD, Jensen JH (2005) Very fast empirical prediction and rationalization of protein pKa values. *Proteins* 61(4):704–721.
17. Bas DC, Rogers DM, Jensen JH (2008) Very fast prediction and rationalization of pKa values for protein-ligand complexes. *Proteins* 73(3):765–783.
18. Sondergaard CR, Olsson MHM, Rostkowski M, Jensen JH (2011) Improved treatment of ligands and coupling effects in empirical calculation and rationalization of pK(a) values. *J Chem Theory Comput* 7:2284–2295.
19. Olsson MHM, Sondergaard CR, Rostkowski M, Jensen JH (2011) PROPKA3: Consistent treatment of internal and surface residues in empirical pK(a) predictions. *J Chem Theory Comput* 7:525–537.
20. Reuter N, Dejaegere A, Maigret B, Karplus M (2000) Frontier bonds in QM/MM methods: A comparison of different approaches. *J Phys Chem A* 104:1720–1735.
21. Dewar MJS, Zoebisch EG, Healy EF, Stewart JJP (1985) The development and use of quantum-mechanical molecular models. 76. AM1 - a new general-purpose quantum-mechanical molecular model. *J Am Chem Soc* 107:3902–3909.
22. Doron D, Major DT, Kohen A, Thiel W, Wu X (2011) Hybrid quantum and classical simulations of the dihydrofolate reductase catalyzed hydride transfer reaction on an accurate semi-empirical potential energy surface. *J Chem Theory Comput* 7:3420–3437.
23. Kaminski GA, Friesner RA, Tirado-Rives J, Jorgensen WL (2001) Evaluation and reparametrization of the OPLS-AA force field for proteins via comparison with accurate quantum chemical calculations on peptides. *J Phys Chem B* 105: 6474–6487.
24. Jorgensen WL, Chandrasekhar J, Madura JD, Impey RW, Klein ML (1983) Comparison of simple potential functions for simulating liquid water. *J Chem Phys* 79:926–935.
25. Torrie GM, Valleau JP (1977) Non-physical sampling distributions in Monte-Carlo free-energy estimation - umbrella sampling. *J Comput Phys* 23:187–199.
26. Kumar S, Bouzida D, Swendsen RH, Kollman PA, Rosenberg JM (1992) The weighted histogram analysis method for free-energy calculations on biomolecules. 1. The method. *J Comput Chem* 13:1011–1021.
27. Verlet L (1967) Computer experiments on classical fluids. 1. Thermodynamical properties of Lennard-Jones molecules. *Phys Rev* 159(1):98–103.
28. Garcia-Viloca M, Truhlar DG, Gao J (2003) Reaction-path energetics and kinetics of the hydride transfer reaction catalyzed by dihydrofolate reductase. *Biochemistry* 42(46):13558–13575.
29. Boekelheide N, Salomón-Ferrer R, Miller TF, 3rd (2011) Dynamics and dissipation in enzyme catalysis. *Proc Natl Acad Sci USA* 108(39):16159–16163.
30. Fierke CA, Johnson KA, Benkovic SJ (1987) Construction and evaluation of the kinetic scheme associated with dihydrofolate reductase from *Escherichia coli*. *Biochemistry* 26(13):4085–4092.
31. Roca M, Oliva M, Castillo R, Moliner V, Tuñón I (2010) Do dynamic effects play a significant role in enzymatic catalysis? A theoretical analysis of formate dehydrogenase. *Chemistry* 16(37):11399–11411.
32. Nam K, Prat-Resina X, Garcia-Viloca M, Devi-Kesavan LS, Gao JL (2004) Dynamics of an enzymatic substitution reaction in haloalkane dehalogenase. *J Am Chem Soc* 126(5): 1369–1376.
33. Roca M, Moliner V, Tuñón I, Hynes JT (2006) Coupling between protein and reaction dynamics in enzymatic processes: Application of Grote-Hynes Theory to catechol O-methyltransferase. *J Am Chem Soc* 128(18):6186–6193.
34. Castillo R, Roca M, Soriano A, Moliner V, Tuñón I (2008) Using Grote-Hynes theory to quantify dynamical effects on the reaction rate of enzymatic processes. The case of methyltransferases. *J Phys Chem B* 112(2):529–534.
35. Ruiz-Pernía JJ, Tuñón I, Moliner V, Hynes JT, Roca M (2008) Dynamic effects on reaction rates in a Michael addition catalyzed by chalcone isomerase. Beyond the frozen environment approach. *J Am Chem Soc* 130(23):7477–7488.
36. Bergsma JP, Gertner BJ, Wilson KR, Hynes JT (1987) Molecular dynamics of a model SN2 reaction in water. *J Chem Phys* 86:1356–1376.
37. Alhambra C, et al. (2001) Canonical variational theory for enzyme kinetics with the protein mean force and multidimensional quantum mechanical tunneling dynamics. Theory and application to liver alcohol dehydrogenase. *J Phys Chem B* 105:11326–11340.
38. Truhlar DG, et al. (2002) The incorporation of quantum effects in enzyme kinetics modeling. *Acc Chem Res* 35(6):341–349.
39. Truhlar DG, et al. (2004) Ensemble-averaged variational transition state theory with optimized multidimensional tunneling for enzyme kinetics and other condensed-phase reactions. *Int J Quantum Chem* 100:1136–1152.
40. Pu J, Gao J, Truhlar DG (2006) Multidimensional tunneling, recrossing, and the transmission coefficient for enzymatic reactions. *Chem Rev* 106(8):3140–3169.
41. Pang JY, Pu JZ, Gao JL, Truhlar DG, Allemann RK (2006) Hydride transfer reaction catalyzed by hyperthermophilic dihydrofolate reductase is dominated by quantum mechanical tunneling and is promoted by both inter- and intramonomeric correlated motions. *J Am Chem Soc* 128(24):8015–8023.
42. Gertner BJ, Wilson KR, Hynes JT (1989) Nonequilibrium solvation effects on reaction rates for model SN2 reactions in water. *J Chem Phys* 90:3537–3558.

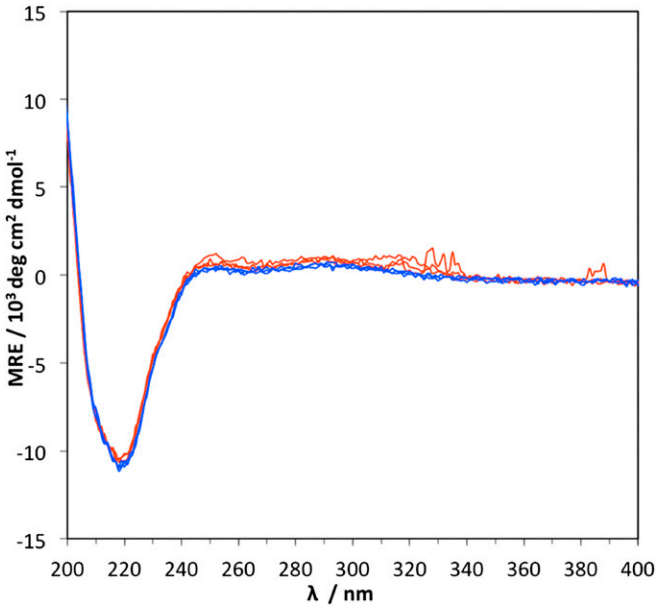

Fig. S1. Circular dichroism spectroscopy of light (red) and heavy (blue) EcDHFR (three scans each), measured in 10 mM potassium phosphate at pH 7, using 14 μM protein.

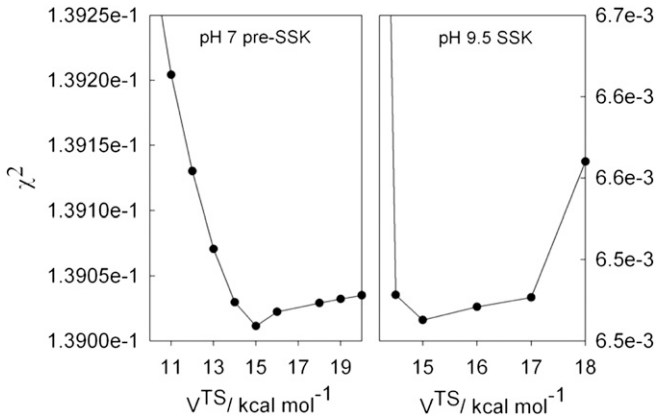

Fig. S2. χ^2 values obtained by fitting the hydride transfer kinetics data to Eq. **3** and Eq. **S1**. The plots were constructed by scanning along V^{TS} and floating all other parameters in Eq. **3** and Eq. **S1**. *Left* and *Right* show χ^2 obtained from fits to the pH 7.0 pre–steady-state kinetic data and the pH 9.5 steady-state kinetic data, respectively. At each pH, the fit shows a χ^2 minimum around $V^{TS} = 15$ kcal·mol^{-1}.

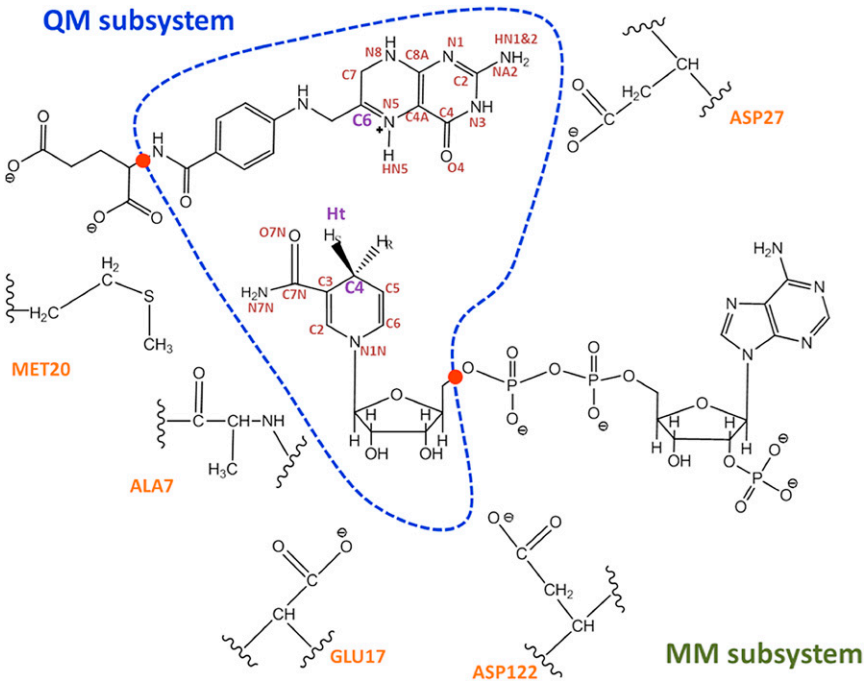

Fig. S3. QM/MM partitioning scheme. Red circles represent the quantum hydrogen link atoms. Atoms in the nicotinamide ring and the pteridine ring, most notably the transferred hydride, Ht, and its donor and acceptor carbon atoms, have been labeled.

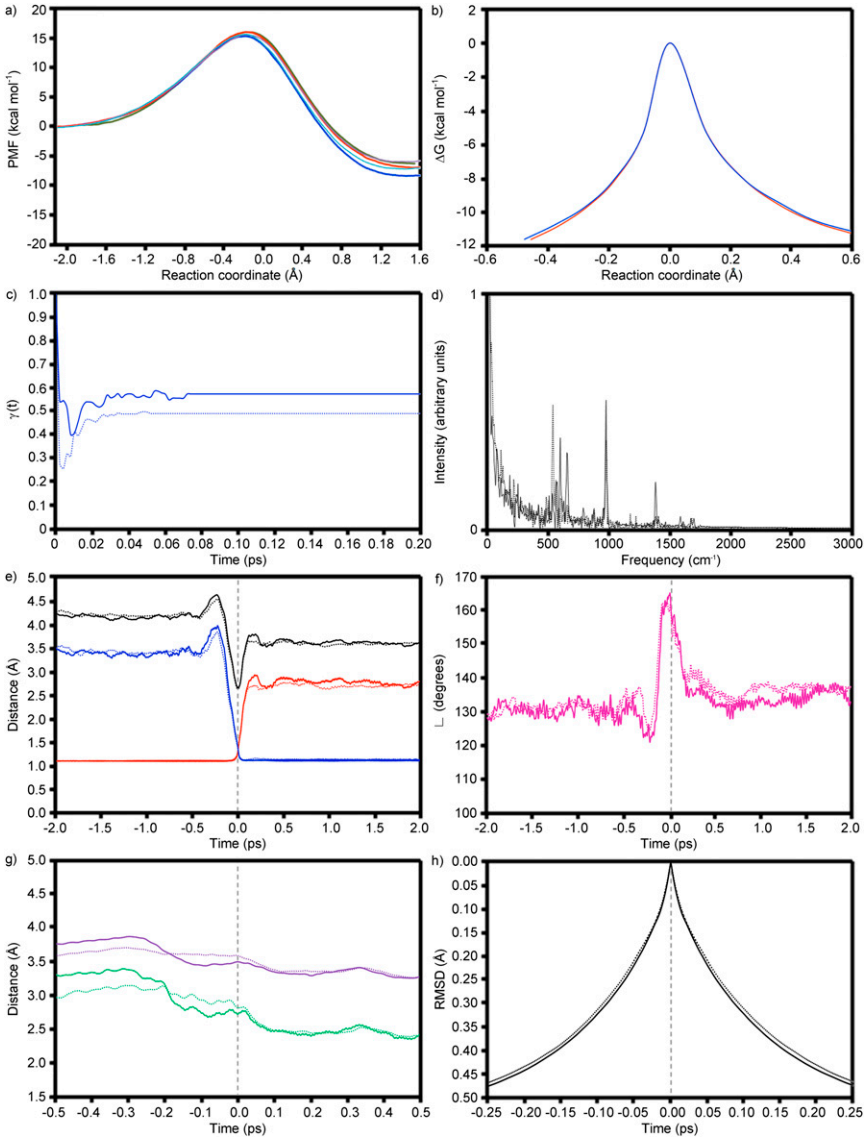

Fig. S4. (*A*) Classical mechanical AM1-SRP/MM potential of mean force (PMF) obtained from five different structures of the TS (different colors are used to indicate PMFs calculated from different starting structures). The starting structures were selected (and subsequently optimized) from a restrained MD simulation of the initial TS structure (main text). This plot shows that the PMFs are well converged. (*B*) Free-energy profiles obtained for the light (red line) and heavy (blue line) enzymes, including the free-energy contribution of the vibrations of the reacting system and surrounding residues to the IRC. The values of the free energy and the reaction coordinate are relative to the light enzyme maxima. This plot shows that the position of the transition state is not affected by variational optimization of the TS; after several trials we found that the change in the position of the variational optimized transition state between the light and heavy enzyme is definitely below 0.01 Å. (*C–H*) Important features of the reaction in the vicinity of the transition state, from simulations of hydride transfer in light (solid lines) and heavy EcDHFR (dashed lines). (*C*) time-dependent evolution of the recrossing transmission coefficients, $\gamma(t)$; (*D*) friction spectra, showing the frequency distribution of motions that are coupled to the reaction coordinate (*SI Text*); (*E*) distances between the C4-C6 (black line), C4-Ht (red line), and C6-Ht (blue line) atoms involved in the chemical reaction; (*F*) angle C4-Ht-C6; (*G*) distances between S_{Met20} and H of $N7N_{NADPH}$ (green line) and between S_{Met20} and $N7N_{NADPH}$ (mauve line); (*H*) averaged evolution of the RMSD (calculated by considering all atoms) from the TS structure in reactive trajectories. For *E–H*, the system is at the top of the barrier at $t = 0$, whereas increasingly negative and positive times correspond to evolution toward the reactant and product states, respectively.

Table S1. Temperature dependence of the steady-state rate constants and enzyme KIEs at pH 9.5 and pH 7 (k_{cat}) and the pre–steady-state rate constants and enzyme KIEs at pH 7 (k_H) for reaction in light and heavy EcDHFR

	Steady state, pH 9.5			Presteady state, pH 7.0			Steady state, pH 7.0		
T (°C)	k_{cat}^{LE}, s^{-1}	k_{cat}^{HE}, s^{-1}	$k_{cat}^{LE}/k_{cat}^{HE}$	k_H^{LE}, s^{-1}	k_H^{HE}, s^{-1}	k_H^{LE}/k_H^{HE}	k_{cat}^{LE}, s^{-1}	k_{cat}^{HE}, s^{-1}	$k_{cat}^{LE}/k_{cat}^{HE}$
7	0.33 ± 0.03	0.32 ± 0.03	1.03 ± 0.07	77.4 ± 1.5	83.7 ± 3.2	0.92 ± 0.04			
10	0.49 ± 0.02	0.43 ± 0.03	1.13 ± 0.04	89.3 ± 1.1	95.9 ± 2.6	0.93 ± 0.01	1.28 ± 0.17	1.31 ± 0.10	0.98 ± 0.09
15	0.80 ± 0.07	0.72 ± 0.07	1.10 ± 0.07	103.1 ± 4.3	113.5 ± 1.7	0.91 ± 0.03	2.12 ± 0.15	2.11 ± 0.17	1.01 ± 0.04
20	1.13 ± 0.15	1.06 ± 0.17	1.06 ± 0.06	119.1 ± 2.7	130.0 ± 1.2	0.92 ± 0.04	3.73 ± 0.11	3.60 ± 0.10	1.04 ± 0.03
25	1.86 ± 0.18	1.64 ± 0.16	1.13 ± 0.08	178.2 ± 4.7	151.6 ± 4.2	1.10 ± 0.03	6.86 ± 0.10	6.49 ± 0.49	1.06 ± 0.01
30	2.76 ± 0.25	2.42 ± 0.24	1.14 ± 0.08	209.1 ± 5.0	190.1 ± 8.5	1.10 ± 0.04	15.53 ± 0.55	13.95 ± 0.38	1.11 ± 0.03
35	3.71 ± 0.23	3.13 ± 0.24	1.18 ± 0.06	248.3 ± 5.3	232.5 ± 3.9	1.07 ± 0.07	23.81 ± 0.31	20.50 ± 0.50	1.16 ± 0.01
40	5.40 ± 0.15	4.25 ± 0.22	1.27 ± 0.04	329.5 ± 19.5	279.5 ± 15.0	1.18 ± 0.09	37.18 ± 0.83	32.33 ± 0.18	1.15 ± 0.02

Table S2. Steady-state kinetic parameters for light and heavy EcDHFR at 20 °C and 35 °C

	pH 9.5		pH 7	
Parameter	Light	Heavy	Light	Heavy
At 20 °C				
k_{cat}, s^{-1}	1.13 ± 0.15	1.06 ± 0.17	3.73 ± 0.11	3.60 ± 0.10
K_M NADPH, μM	1.86 ± 0.20	1.89 ± 0.30	5.10 ± 0.74	4.04 ± 0.39
K_M DHF, μM	1.15 ± 0.27	1.29 ± 0.34	1.05 ± 0.12	0.53 ± 0.08
At 35 °C				
k_{cat}, s^{-1}	3.71 ± 0.23	3.13 ± 0.24	23.8 ± 0.3	20.5 ± 0.5
K_M NADPH, μM	6.54 ± 1.47	5.74 ± 0.74	11.5 ± 2.6	11.3 ± 2.2
K_M DHF, μM	3.73 ± 0.88	2.78 ± 0.86	1.47 ± 0.12	1.56 ± 0.37

Table S3. pH dependence of the pre–steady-state rate constant (k_H) for reaction in light and heavy EcDHFR at 20 °C and 35 °C

	20 °C		35 °C	
pH	k_H^{LE}, s^{-1}	k_H^{HE}, s^{-1}	k_H^{LE}, s^{-1}	k_H^{HE}, s^{-1}
9	0.72 ± 0.02	0.75 ± 0.08	5.9 ± 0.3	3.4 ± 0.3
8.5	22.0 ± 1.3	23.5 ± 3.8	38.7 ± 1.1	32.0 ± 0.9
8	30.2 ± 0.9	33.3 ± 2.2	107.5 ± 1.1	104.9 ± 1.5
7.5	64.0 ± 1.0	57.9 ± 1.2	163.8 ± 2.1	158.5 ± 1.1
7	152.5 ± 1.5	156.7 ± 2.5	248.3 ± 5.3	232.5 ± 3.9
6.5	207.7 ± 5.7	216.3 ± 3.1	425.4 ± 7.0	416.5 ± 3.7
6	306.0 ± 6.8	317.2 ± 3.1	530.5 ± 17.2	535.5 ± 14.5
5.5	365.0 ± 9.5	377.0 ± 3.5	1,157.0 ± 25.0	1,149.0 ± 57.8
5	447.1 ± 26.5	437.3 ± 4.5	1,400.3 ± 70.0	1,274.0 ± 120.0

Table S4. Best set of parameters giving the fits shown in Fig. 2 of the main text, using Eq. 3 and Eq. S1

	Using Eq. **3** and Eq. **S1***		Arrhenius-like fits†	
Parameters	pH 7	pH 9.5	pH 7	pH 9.5
C^{LE}, $K^{-1}\cdot s^{-1}$	$1.11^{+51.9}_{-1.10}\times10^{9}$	$1.31^{+2.86}_{-1.30}\times10^{9}$	$2.46^{+1.55}_{-1.55}\times10^{4}$	$5.14^{+2.05}_{-2.05}\times10^{7}$
C^{HE}, $K^{-1}\cdot s^{-1}$	$1.03^{+47.5}_{-1.02}\times10^{9}$	$1.15^{+2.31}_{-1.14}\times10^{9}$	$2.46^{+1.55}_{-1.55}\times10^{4}$	$4.55^{+1.07}_{-1.07}\times10^{7}$
ε^{LE}, kcal·mol^{-1}	$14.6^{+10.1}_{-10.1}$	$16.2^{+1.82}_{-1.82}$	$6.33^{+0.37}_{-0.37}$	$13.57^{+0.24}_{-0.24}$
ε^{HE}, kcal·mol^{-1}	$14.6^{+9.5}_{-9.5}$	$16.2^{+1.82}_{-1.82}$	$6.33^{+0.35}_{-0.35}$	$13.57^{+0.21}_{-0.21}$
V^{TS}, kcal·mol^{-1}	15.0‡	15.0‡	—	—
ω^{LE}, cm^{-1}	1296^{+408}_{-408}	1000^{+204}_{-204}	—	—
ω^{HE}, cm^{-1}	1296^{+388}_{-388}	1000^{+189}_{-189}	—	—

Errors shown are SEs (σ) obtained during the least-squares fitting procedure. The uncertainty in some of the parameters is large, owing to considerable parameter codependency; see *SI Text* for a discussion of errors and parameter covariance.
*In these fits, all of the parameters were floated.
†In these fits, we constrained $\kappa^{HE}(T) = \kappa^{LE}(T) = 1$ in Eq. **3**, giving an Arrhenius-like fit of the form $CT\exp(-\varepsilon/RT)$.
‡Value was fixed at 15.0 to correspond to the χ^2 minima obtained in relaxed scans (Fig. S2).

Table S5. Key averaged structural parameters of the reactant state, RS, and transition state, TS, from 2-ns MD simulations at the AM1-SRP/MM level of the RS and the TS at 300 K

Parameter	RS	TS
Reaction coordinate: (C_{donor}-H)-($C_{acceptor}$-H)	−1.95 ± 0.36	−0.17 ± 0.04
Distance C_{donor}-$C_{acceptor}$	3.93 ± 0.25	2.63 ± 0.06
Distance C_{donor}-H	1.09 ± 0.03	1.25 ± 0.03
Distance $C_{acceptor}$-H	3.05 ± 0.36	1.41 ± 0.04
Angle C_{donor}-H-$C_{acceptor}$	141 ± 15	163 ± 7
Distance $OD2_{ASP27}$-$N3_{substrate}$	2.74 ± 0.12	2.82 ± 0.16
Distance $OD1_{ASP27}$-NA2 $_{substrate}$	2.81 ± 0.14	2.76 ± 0.12
Distance S_{MET20}-$N7N_{cofactor}$	4.30 ± 0.50	3.40 ± 0.30
Distance S_{MET20}-$N5_{substrate}$	3.76 ± 0.35	3.70 ± 0.33
Distance O_{ALA7}-$N7N_{cofactor}$	3.68 ± 0.28	3.11 ± 0.19
Distance O_{ALA7}-S_{MET20}	6.36 ± 0.48	5.93 ± 0.41

Distances are in angstroms and angles in degrees.